

See discussions, stats, and author profiles for this publication at: <https://www.researchgate.net/publication/281762074>

Pixeled Electroluminescence from Multilayer Heterostructure Organic Light-Emitting Transistors

ARTICLE *in* THE JOURNAL OF PHYSICAL CHEMISTRY C · AUGUST 2015

Impact Factor: 4.77 · DOI: 10.1021/acs.jpcc.5b04708

READS

3

5 AUTHORS, INCLUDING:



Yongsheng Hu

Changchun Institute of Optics, Fine Mechanics...

6 PUBLICATIONS 17 CITATIONS

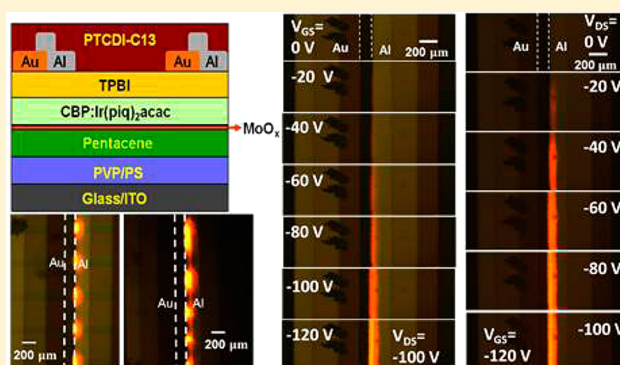
SEE PROFILE

Pixelated Electroluminescence from Multilayer Heterostructure Organic Light-Emitting Transistors

Li Song,^{†,‡} Yongsheng Hu,^{*,†} Dongwei Li,^{†,‡} Hong Chen,[§] and Xingyuan Liu^{*,†}[†]State Key Laboratory of Luminescence and Applications, Changchun Institute of Optics, Fine Mechanics and Physics, Chinese Academy of Sciences, Changchun 130033, China[‡]University of Chinese Academy of Sciences, Beijing 100049, China[§]Key Laboratory of Optical System Advanced Manufacturing Technology, Chinese Academy of Sciences, Changchun 130033, China

Supporting Information

ABSTRACT: Improved performance of multilayer heterostructure organic light-emitting transistors (OLETs) was observed in brightness and external quantum efficiency (EQE) by inserting an ultrathin MoO_x layer and TPBI buffer layer. With in-plane emission mainly beneath the drain electrode with a maximum width of 120 μm, an EQE of 0.16% at a brightness of 238 cd/m² was obtained. Different sizes of pixelated OLETs were fabricated by restricting the pixel length by narrowing the width of the gate electrode perpendicular to the source/drain electrodes. Light emission pixels with sizes from 25 to 400 μm have been successfully demonstrated. The maximum width of the emission zone was not affected, and the maximum EQE and the corresponding brightness presented an increasing tendency for pixelated OLETs. The results in our work are helpful for developing a new generation of OLET-based display technology.



1. INTRODUCTION

Organic light-emitting transistors (OLETs) are a novel class of multifunctional optoelectronic devices that combine the light emission function of an organic light-emitting diode (OLED) with the switching function of a transistor.^{1,2} This multifunctional property ensures their wide application such as in flat-panel displays and optical communication systems, because a much simpler fabrication process and high level of integration can be achieved.^{3–6} Generally, for OLET-based display technology, the OLETs should have a spatially stable light emission area and a tunable width between 20 and 400 μm to achieve a favorable aperture ratio in the pixel. Meanwhile, a high external quantum efficiency (EQE) at high brightness, and a large on/off ratio (>100) are also prerequisites for OLET displays.⁷

High EQE can be obtained in the ambipolar single-layer OLETs because of the balanced concentration of holes and electrons.^{8–11} However, the width of the light emission zone is significantly limited because both holes and electrons would accumulate in the same organic/dielectric interface.^{12–14} Multilayer OLETs,^{15–24} especially the trilayer structure consisting of a p-channel/emitter/n-channel heterostructure,^{20,25,26} can allow carrier transport in different active layers along the channel under appropriate bias voltages, thus providing a wider emission width compared with the single-layer OLETs. Toffanin et al. observed full channel illumination in trilayer OLETs based on small molecular semiconductors.²⁶

Kajii et al. also achieved in-plane channel emission in bilayer OLETs utilizing two polymers.^{17,27} Though their studies present promising applications for flat-panel displays in terms of plane illumination, the limited on/off ratios (<10) are far from sufficient, and the voltage dependence of the light-emitting location is also inconvenient for pixelated emission, which requires a spatially stable light emission area. Mujeeb et al. realized intensive light emission located in the source/drain (S/D) electrodes by implementing nonplanar asymmetric electrodes.²⁷ The high EQE at high brightness as well as the large on/off ratio manifest that heterostructure OLETs with unipolar characteristics can not only obtain in-plane light emission but also provide a spatially stable illumination area with promising performance. Despite these important advances, more related studies are worth continuing, especially for molecular multilayer heterostructure OLETs because of their high flexibility in material selection and great potential in improving overall performance.

In this study, we present a multilayer OLET with enhanced performance based on the use of a transition metal oxide, MoO_x, as the interface modification layer, and TPBI as the buffer layer, as well as asymmetric electrodes to improve the injection of electrons. The devices exhibit unipolar character-

Received: May 18, 2015

Revised: August 5, 2015

Published: August 12, 2015

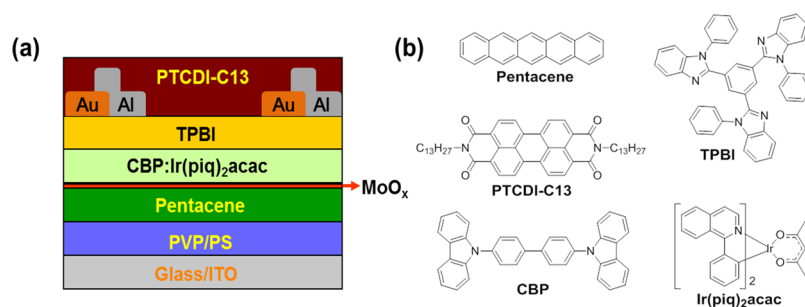


Figure 1. (a) Schematic of a typical OLET. (b) Molecular structures of the organic materials.

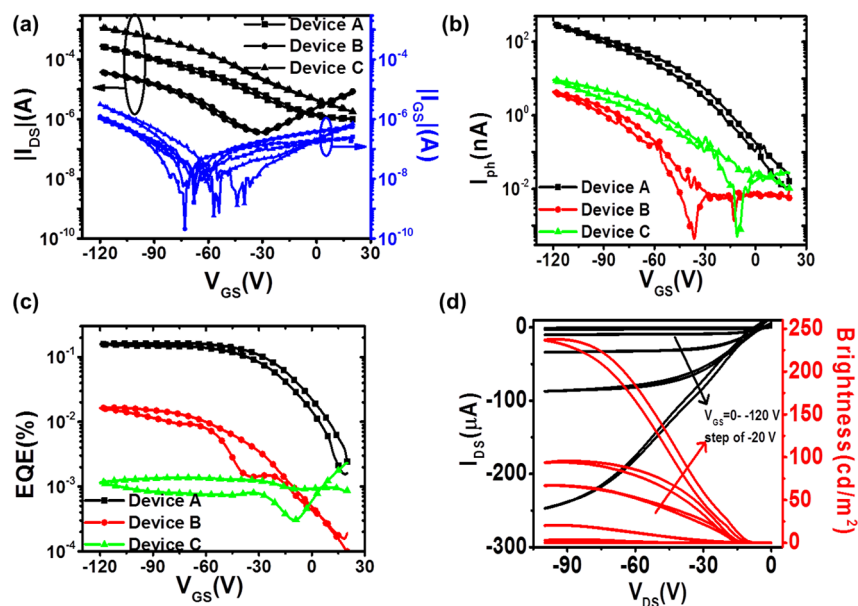


Figure 2. (a) Transfer characteristics ($V_{DS} = -100$ V) of devices A, B, and C. (b) The photocurrent and (c) the EQE corresponding to the transfer characteristics. (d) The output characteristics of device A along with the corresponding brightness when V_{GS} varies from 0 to -120 V.

istics. We observed a spatially stable in-plane light emission location mainly underneath the electron injection electrode. We further realized pixelated light emission with different sizes, whose length is determined by the width of the gate electrode. Our results suggest that multilayer OLETs with unipolar characteristics are capable of realizing high-performance pixelated light emission, which is promising for application in the next generation of OLET-based display technology.

2. EXPERIMENTAL SECTION

The device architecture of a typical OLET, called device A, is shown in Figure 1a. Simultaneously an OLET without MoO_x (device B) and an OLET without TPBI (device C) were fabricated as control devices to clarify the functions of MoO_x and TPBI layers. The molecular structures of the materials used in this study are shown in Figure 1b. Indium tin oxide (ITO) on the glass substrate was used as the gate electrode to facilitate light emission from the substrate side. The dielectric layer was made up of 350 nm poly-4-vinylphenol (PVP) and 30 nm polystyrene (PS), which was prepared by spin-coating in a method reported elsewhere.²⁸ Pentacene (15 nm), MoO_x (0.25 nm), CBP:Ir(piq)₂acac (weight concentration of approximately 6%) (20 nm), and TPBI (14 nm) were successively thermal-evaporated at rates of 0.2, 0.05, 2, and 0.2 Å/s, respectively. The asymmetric source and drain electrodes were evaporated at a deposition rate of 0.3 Å/s by rotating the substrates at a fixed

angle to control the channel length to be 120 μm and a channel width 3 mm through a shadow mask, followed by the deposition of PTCDI-C13 (P13, 30 nm) at a rate of 0.5 Å/s. All devices were encapsulated with UV glue in the glovebox (H_2O , $\text{O}_2 < 0.1$ ppm) prior to the performance test.

The electrical characteristics were evaluated by a Keithley 4200 SCS at room temperature under ambient air. The photocurrent (I_{ph}) was collected by a HAMAMATSU S1336 photodiode. The channel image was captured by an Olympus BX51TRF CCD microscope with a 20 \times objective lens. The electroluminescence (EL) spectra were acquired by an AvaSpec-ULS2048L fiber spectrometer. The carrier mobilities were calculated by the formula for the saturation regime: $I_{DS} = \mu C_i (W/2L)(V_{GS} - V_T)^2$, where μ is the field-effect mobility, C_i is the gate dielectric capacitance density, V_T is the threshold voltage, V_{GS} is the gate-source voltage, and W and L are the channel width and length, respectively. The EQE was calculated as follows

$$\text{EQE} = \frac{P_{\text{tot}}/E_{ph}}{I/q} = \frac{P_{\text{tot}}(W)}{I(A)E_{ph}(\text{eV})} = \frac{I_{ph}/K(A/W)}{I_{DS}E_{ph}(\text{eV})} \approx 1.5 \frac{I_{ph}}{I_{DS}} \quad (1)$$

where P_{tot} , K , E_{ph} , I_{ph} , I_{DS} , and q are the total emitted light power, photosensitivity of the detector (0.3 A/W), average

Table 1. Characteristics for Different OLETs: Average Values for at Least Five Devices

device/width of gate electrode (μm)	max I_{ph} (nA)	max width of recombination zone (μm)	max EQE (%)	recombination efficiency at maximum EQE (%)	max brightness (cd/m^2)	on/off ratio
A	300 ± 6	120 ± 5	$1.6 \pm 0.3 \times 10^{-1}$	1.6 ± 0.3	200 ± 5	$3 \pm 0.1 \times 10^2$
B	5 ± 1	70 ± 5	$1.4 \pm 0.1 \times 10^{-3}$	$1.4 \pm 0.1 \times 10^{-2}$	12 ± 3	$2 \pm 0.5 \times 10^1$ for electron, $1 \pm 0.1 \times 10^3$ for hole
C	10 ± 1	70 ± 10	$1.6 \pm 0.4 \times 10^{-2}$	$1.6 \pm 0.4 \times 10^{-1}$	6 ± 2	$7 \pm 0.4 \times 10^2$
400	60 ± 5	120 ± 5	$2.8 \pm 0.2 \times 10^{-1}$	2.8 ± 0.2	300 ± 10	$5 \pm 1 \times 10^1$
200	30 ± 5	120 ± 5	$2.8 \pm 0.2 \times 10^{-1}$	2.8 ± 0.2	300 ± 10	$2 \pm 1 \times 10^1$
100	15 ± 5	120 ± 5	$2.5 \pm 0.5 \times 10^{-1}$	2.5 ± 0.5	300 ± 10	$1 \pm 0.3 \times 10^1$
50	6 ± 4	120 ± 5	$2.0 \pm 0.5 \times 10^{-1}$	2.0 ± 0.5	250 ± 20	$5 \pm 1 \times 10^0$
25	3 ± 1	120 ± 5	$1.2 \pm 0.3 \times 10^{-1}$	1.2 ± 0.3	200 ± 10	$3 \pm 1 \times 10^0$

photon energy, photon current, drain current, and electron charge, respectively. The brightness was calculated by comparing the photocurrent with a standard OLED of known brightness ($1000 \text{ cd}/\text{m}^2$) and light-emission area ($3 \text{ mm} \times 1 \text{ mm}$) with a structure of ITO/NPB (20 nm)/CBP:Ir(piq)₂acac (20 nm)/TPBI (30 nm)/LiF (1 nm)/Al (100 nm).

3. RESULTS AND DISCUSSION

We first investigated the influence of MoO_x and TPBI on the device performance. The transfer characteristics of the three devices are shown in Figure 2a. Device A exhibits a typical p-type transistor characteristic, which is also demonstrated in its output curve as shown in Figure 2d. The hole mobility is $0.58 \text{ cm}^2/(\text{V s})$. The drain current (I_{DS}) decreases as the V_{GS} changes from -120 to 20 V , and tends to be stable with an on/off ratio of approximately 300. Device B represents ambipolar characteristics with a hole current lower by approximate 1 order of magnitude compared with that of device A. The output characteristic of device B is shown in Figure S1 (in the Supporting Information). The hole and electron mobilities are 0.08 and $0.012 \text{ cm}^2/(\text{V s})$, respectively. Device C exhibits similar electrical characteristics to device A, but with higher hole mobility ($1.9 \text{ cm}^2/(\text{V s})$), hole current, and on/off ratio (see Table 1). In comparing device A with device B, it is notable that the extremely thin MoO_x layer can increase the hole current clearly, and change the polarity of the device from bipolarity to unipolarity. The decrease in hole current of device A compared with that of device C was due to the higher value of the highest occupied molecular orbital (HOMO) level of TPBI (6.7 eV), which blocks the holes.

Because the high gate leakage current may also lead to light emission, we plotted the gate leakage current (I_{GS}) vs V_{GS} in Figure 2a. Fortunately, there seems to be no relationship between I_{GS} and I_{ph} , because device B has the largest I_{GS} but the smallest I_{ph} . The position of the emission zone fixed at the electrode (analyzed below) would probably be more evidence to rule out the leakage current as a possible origin for the light emission, because the leakage current would spread over the entire channel, which would result in light emission in the channel. Hence, the effect of the gate leakage current in our research can be neglected. The I_{ph} and EQE corresponding to the transfer curves are shown in Figure 2b,c, respectively. All the devices obtain their own maximum I_{ph} under the voltage bias of $V_{\text{GS}} = -120 \text{ V}$, $V_{\text{DS}} = -100 \text{ V}$, where holes dominate. For device A, the maximum I_{ph} is up to 300 nA along with a maximum EQE of 0.16% , and the EQE tends to be saturated when V_{GS} changes from -40 to -120 V . For device B, the maximum I_{ph} is only 5 nA , which is much smaller than that of device A. Although device B exhibits bipolar transport

characteristics, an extremely weak I_{ph} less than 1 nA is detected in the electron dominated region, i.e., V_{GS} from -30 to 20 V . The EQE as a function of V_{GS} does not exhibit the feature of typical ambipolar OLETs where EQE is a maximum in the carrier-balanced region.^{29–31} The phenomenon in which EL occurs in correspondence to the hole transportation and is proportional to the hole current is similar to that of bilayer heterostructure OLETs,³² which indicates that the EL characteristics are probably related to the charge transport in the layer directly in contact with the dielectric layer. Hence, in our devices, hole transport finally determined the EL characteristics. Therefore, it is crucial for the thin MoO_x layer to improve the hole current and the EL intensity.

Regarding device C, the maximum I_{ph} is 10 nA . However, the EQE is 2 orders of magnitude lower compared with that of device A, and 1 order of magnitude lower than that of device B. We plot the relationship between EQE and current densities in Figure S2. The EQE values for all the devices did not show any decrease at higher current densities. There are several reasons for the low I_{ph} and EQE: (a) Stronger exciton quenching results from the electron-injection electrode because of the direct contact between the emission layer and the electrode without a TPBI buffer layer; (b) the large barrier between PTCDI-C13 and CBP restricts the transportation of electrons from the lowest unoccupied molecular orbital (LUMO) level of PTCDI-C13 to that of CBP; (c) higher hole current leads to intensive charge–exciton interaction without the hole-blocking layer of TPBI.

Although we have shown significant improvement for the EQE by incorporating both MoO_x and TPBI, it is still much lower compared with the corresponding OLED in the literature. We believe that this is mainly due to the unbalanced carrier injection and transportation because the emission zone is mainly underneath the electrode, which would probably induce metal–exciton quenching. Furthermore, the large barrier (1.0 eV ; see Figure 4a) between the hole transport layer (pentacene) and emissive layer (CBP:Ir(piq)₂acac) blocks the hole injection from pentacene to CBP, which would result in less efficient exciton formation.

Figure 2d presents the output characteristics of device A along with the corresponding brightness. We did not show the brightness corresponding to the transfer characteristics as the illumination area changed significantly when various V_{GS} were applied to the devices at fixed V_{DS} , which is discussed in more detail below. Both the drain current and brightness depend on the bias voltages. For each fixed V_{GS} , the I_{DS} and brightness become saturated at high V_{DS} . The maximum brightness is approximately $238 \text{ cd}/\text{m}^2$.

The efficiency of light emission can be calculated as⁸

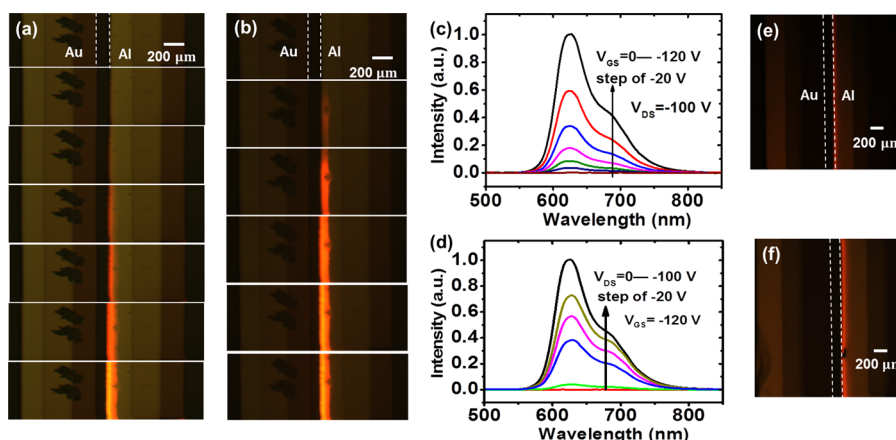


Figure 3. (a) Optical microphotographs of the emission zone of device A under $V_{DS} = -100$ V with V_{GS} varying from 0 to -120 V at the step of -20 V from the top to the bottom. (b) Optical microphotographs of the emission area of device A under $V_{GS} = -120$ V with V_{DS} varying from 0 to -100 V at the step of -20 V from the top to the bottom. (c) EL spectra for device A corresponding to (a). (d) EL spectra for device A corresponding to (b). (e) Optical microphotographs of the emission area of device B (e) and device C (f) under $V_{DS} = -100$ V and $V_{GS} = -120$ V.

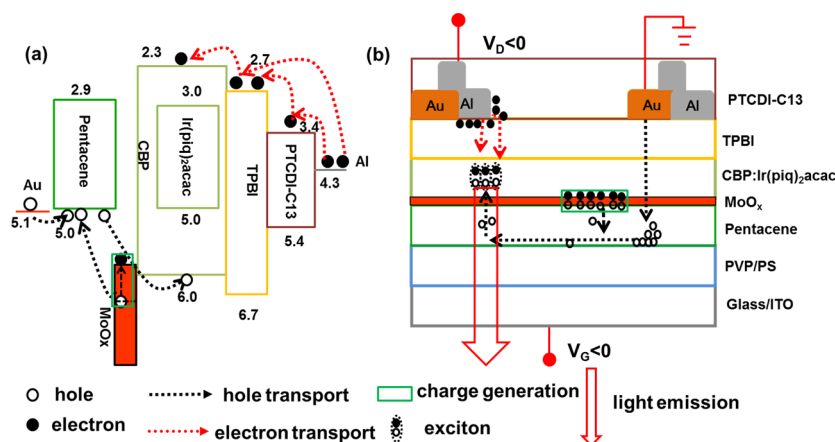


Figure 4. (a) Energy schematic diagram for the devices. (b) Schematic representations of the carrier injection and transport.

$$\Phi_{EQE} = \Phi_{out} \times \Phi_{spin} \times \Phi_{PL} \times \Phi_{rad} \quad (2)$$

where Φ_{out} is the outcoupling efficiency determining the fraction of generated light that can be measured outside the device, Φ_{spin} is a factor to take account of spin statistics, Φ_{PL} is fluorescent quantum efficiency, and Φ_{rad} is the recombination efficiency. For our devices, $\Phi_{out} = 20\%$,³³ $\Phi_{spin} = 1$ (for OLETs with phosphorescent material as the emission layer³⁴), $\Phi_{PL} = 50\%$,³⁵ and Φ_{EQE} is the calculated EQE; therefore, the calculated recombination efficiency Φ_{rad} for device A is 1.6%, which is approximately 100 times larger than that of the device B and approximately 10 times that of the device C (see Table 1). The calculated Φ_{rad} data in Table 1 provide reference valuable for recombination efficiency, which would be lower than the actual value when considering the factor that spin statistic 1 is nearly impossible in real OLEDs. The large differences in the efficiency of electron–hole capture eventually result in the differences in EQE between the devices. Therefore, both the MoO_x and the TPBI make contributions to the electron–hole capture. There are some important reasons to interpret the contributions: (a) The MoO_x increases the hole current significantly, which is extremely important for the EL characteristics. (b) The existence of a TPBI buffer layer avoids direct contact between the emission layer and electrodes, which will abate the exciton–metal quenching effect. (c) The LUMO

level of TPBI lying between that of the CBP and PTCDI-C13 facilitates charge percolation from the electron transport layer to the emission layer; hence, the device structure promotes the exciton formation. (d) The high LUMO level of TPBI plays a role in blocking holes, and the exciton–charge quenching is also simultaneously hindered to some extent.

In Figure 3a we show the optical microphotographs of the emission area when the device A is biased at constant $V_{DS} = -100$ V with V_{GS} varying from 0 to -120 V at a step of -20 V. We profiled the emission intensity across the transistor channel and partial electrodes to obtain the emission zone width (full width at half-maximum (fwhm)) at $V_{DS} = -100$ V with different V_{GS} values (see Figure S3). It is obvious that the light emission is located mainly underneath the electron injection electrode. With the V_{GS} increasing negatively, not only does the brightness enhance gradually but also the emission area extends progressively. The emission zone mainly extends beneath the electrode. Simultaneously, an extremely narrow extension, less than $10 \mu m$, was observed in the channel. The emission zone reaches its largest size (approximately $120 \mu m$) at $V_{GS} = -120$ V. We also investigated the light emission area of devices B and C, for which the microphotographs are shown in Figure 3e,f, at $V_{GS} = -120$ V and $V_{DS} = -100$ V. The widths underneath the drain electrode are approximately $70 \mu m$ for device B and approximately $75 \mu m$ for device C, respectively. The extension

in the channel is approximately $10\ \mu\text{m}$ for both devices. This phenomenon indicates that MoO_x and TPBI play a collaborative role in extending the light emission zone.

The optical microphotographs of the emission zone are shown in Figure 3b, when the device A is biased at constant $V_{\text{GS}} = -120\ \text{V}$ with V_{DS} varying from 0 to $-100\ \text{V}$ at a step of $-20\ \text{V}$. In contrast to the extension that varies from 0 to $120\ \mu\text{m}$ when V_{GS} changes from 0 to $-120\ \text{V}$ at a certain definite V_{DS} , the emission zone extends in a smaller region from 90 to $120\ \mu\text{m}$ when V_{DS} changes from 0 to $-100\ \text{V}$ at a certain definite V_{GS} . The light intensity is enhanced significantly as the V_{DS} negatively increases, which is similar to that when changing V_{GS} . Because the emission zone highlights the charge carrier recombination zone, the features observed indicate that the influence of V_{GS} on the carrier distribution is much stronger than that of V_{DS} .

EL spectra for device A are shown in Figure 3c,d. It can be seen that the positions of the main peaks and the profile of the EL spectra are nearly identical to that of $\text{CBP}:\text{Ir}(\text{piq})_2\text{acac}$ reported elsewhere,^{36,37} which suggests the same excitations independent of the bias voltages.

To better understand the operating mechanism, we depict the energy schematic diagram and schematic representations of the carrier injection and transport in Figure 4. Here, we assume that there are charges generated in the MoO_x layer, because spontaneous electron transfer can occur in a vacuum-deposited MoO_x layer from various defect states to the conduction band via thermal diffusion.³⁸ When the devices are operating in the hole accumulation mode ($V_{\text{GS}} < 0$), the holes are injected from the Au/source electrode via the HOMO levels of TPBI and emission layers and transport subsequently in the pentacene layer. Meanwhile, the MoO_x near the source electrode will bear forward voltage bias in the vertical direction. Assisted by the strong electrical field, the generated holes can be injected via thermal diffusion from MoO_x to the HOMO level of pentacene. The electrons generated by spontaneous transfer in MoO_x are unlikely to inject into the LUMO level of CBP because of the large barrier, as shown in Figure 4a, and may be captured by the injected holes from the source electrode, and hence, the MoO_x returns to the initial states, which can generate holes and electrons. The total result shows that MoO_x facilitates the hole injection by generating holes and electrons, which probably is the main reason for the notable increase in the hole current. The electrons are partially injected into PTCDI-C13 from the edge of the Al/drain electrode and then to the TPBI buffer layer, and partially injected to the TPBI layer directly because of the low work function of the Al electrode, as shown in Figure 4b. To validate the electron injection from the electrode into P13, we made two control devices with configurations of ITO/PVP/PS/pentacene/ MoO_x /CBP: $\text{Ir}(\text{piq})_2\text{acac}$ /TPBI/P13/Au/Al (control A) and ITO/PVP/PS/pentacene/ MoO_x /CBP: $\text{Ir}(\text{piq})_2\text{acac}$ /TPBI/Au/Al (control B). Figure S4 shows the transfer curves together with the I_{ph} and EQE for control A and control B. Both the electrical and optical performance of control A decreased compared with those of device A, which is probably due to the hole block function of P13 when it was placed under the source and drain electrodes. The maximum hole current of control B exhibits no apparent difference compared with that of the standard device, whereas the decrease of photocurrent and EQE indicates the reduction of injected electrons. Therefore, we speculate that the electrons can be injected into P13 when it is on top of the source and drain electrodes. Excitons are generated from the charge

percolation of holes moving across the channel and the injected electrons into the emissive layers, which finally results in the intense light emission beneath the drain electrode.

OLETs with different widths of the gate electrode (W_{g}) based on the standard structure were fabricated to show their potential application in OLET-based display technology. We prepared two types of ITO arrays: one contains five $100\ \mu\text{m}$ ITO gate electrodes and the other consists of five different ITO gate electrodes whose widths are 25, 50, 100, 200, and $400\ \mu\text{m}$. The length of the light emission area is determined by W_{g} by intersecting the S/D electrodes and the gate electrodes perpendicularly (see Figure S5). Figure 5a shows a micro-

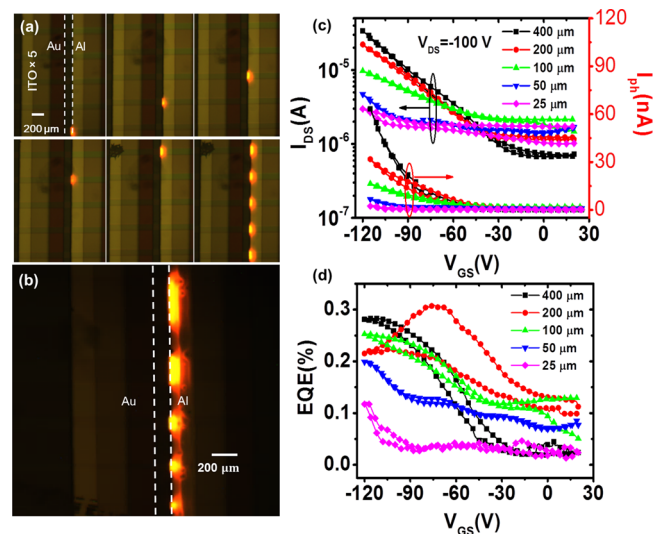


Figure 5. (a) Microphotographs of an OLET array with $100\ \mu\text{m}$ W_{g} ; the pixels are lit one by one and lit together at $V_{\text{DS}} = -100\ \text{V}$, $V_{\text{GS}} = -120\ \text{V}$. (b) Microphotographs of an OLET array with different W_{g} values (400, 200, 100, 50, and $25\ \mu\text{m}$ from the top to the bottom). (c) Transfer characteristics and the corresponding photocurrent. (d) EQE of OLETs with different W_{g} values.

photograph of the $100\ \mu\text{m} \times 1$ array at $V_{\text{DS}} = -100\ \text{V}$ and $V_{\text{GS}} = -120\ \text{V}$, including lighting the five OLETs separately and together. It can be observed that the light emission area of each pixel is about $100 \times 120\ \mu\text{m}^2$ (neglecting the emission beyond the ITO area). The width of the emission zone is in accordance with that of device A; other parameters can be found in Table 1.

Microphotographs of OLETs with different W_{g} values are shown in Figure 5b at $V_{\text{DS}} = -100\ \text{V}$ and $V_{\text{GS}} = -120\ \text{V}$. It is obvious that the change of gate width brings negligible influence on the location and extension of the emission. At high drain current, the values of $I_{\text{DS}}/W_{\text{g}}$ remain almost identical to each other. Figure 5c shows their transfer characteristics along with the corresponding photocurrent. When the I_{DS} starts to increase sharply, the value of V_{GS} increases negatively as W_{g} decreases, which is probably caused by the larger resistance of the narrower gate electrode; i.e., the total line resistance of the $25\ \mu\text{m}$ gate electrode reaches more than $6\ \text{k}\Omega$. The increasing gate electrode resistance results in a high threshold voltage and low I_{ON} in the same region ($V_{\text{GS}} = -120$ to $20\ \text{V}$), thus finally leading to a small on/off ratio. The EQE as a function of V_{GS} is shown in Figure 5d. The EQE exhibits unsaturation, and the maximum EQE for each device is larger than that of device A

except for the device with a 25 μm gate electrode, which can be attributed to the increased threshold voltage.

For OLET-based display technology, an important parameter is the aperture ratio, a ratio between the illuminated and the total area of a pixel. It is unfortunate that the ratios for different W_g values we obtain from the definition were extremely low: 4.5% for 400 μm , 3.1% for 200 μm , 1.9% for 100 μm , 1.1% for 50 μm , and 0.60% for 25 μm . However, this is mainly a result of the preparation process we implemented. The aperture ratio can be dramatically improved by decreasing the width of the S/D electrodes (1.4 mm in total for our devices), the channel length (120 μm in our devices), and the distance between the neighboring gate electrodes (300 μm used to calculate the aperture ratio). As shown in Figure 5b, another important issue is the crosstalk between the neighboring pixels, which is probably due to the total coverage of the active layer on the substrate. Methods such as depositing the active layer via a well-designed shadow mask and introducing isolation made of insulators^{39,40} can reduce the crosstalk to some extent.

4. CONCLUSIONS

The EL performance of multilayer heterostructure OLETs was enhanced via effective interfacial modifications. We have observed spatially stable in-plane emission mainly beneath the electron injection electrode, and the extensions of the light emission region can be tuned by the bias voltage with the maximum width of 120 μm . An EQE of 0.16% at 238 cd/m^2 was obtained in our typical OLETs. Further, we have demonstrated light emission pixels with different sizes from 25 to 400 μm by means of limiting the width of the gate electrode, which determines the length of the illumination area eventually. The emission zone locations are also spatially stable, and the maximum widths remain identical to the typical device. The EQE as well as brightness exhibit an increasing tendency as the gate electrodes become narrow. Though the performance of our pixelated OLETs remains to be improved, the multilayer heterostructure unipolar OLETs with spatially stable in-plane light-emitting characteristics are anticipated to be useful for the next generation of OLET-based display technology.

■ ASSOCIATED CONTENT

Supporting Information

The Supporting Information is available free of charge on the ACS Publications website at DOI: 10.1021/acs.jpcc.5b04708.

- (1) The output characteristics of device B to confirm the saturation regime.
- (2) EQE vs channel current densities for devices A, B, and C.
- (3) Light emission intensity profile and emission zone width.
- (4) Transfer characteristics, corresponding photocurrent, and EQE for control devices.
- (5) Schematic of two types of ITO arrays (PDF)

■ AUTHOR INFORMATION

Corresponding Authors

*Phone: +86-431-86176342. E-mail: liuxy@ciomp.ac.cn (X.L.).

*Phone: +86-431-86176341. E-mail: huyongsheng@ciomp.ac.cn (Y.H.).

Notes

The authors declare no competing financial interest.

■ ACKNOWLEDGMENTS

The work was supported by the CAS Innovation Program, and the National Natural Science Foundation of China through

Grant No. 6140031454, and a project supported by the State Key Laboratory of Luminescence and Applications.

■ REFERENCES

- (1) Cicoira, F.; Santato, C. Organic Light Emitting Field Effect Transistors: Advances and Perspectives. *Adv. Funct. Mater.* **2007**, *17*, 3421–3434.
- (2) Santato, C.; Cicoira, F.; Martel, R. Organic Photonics Spotlight on Organic Transistors. *Nat. Photonics* **2011**, *5*, 392–393.
- (3) Wakayama, Y.; Hayakawa, R.; Seo, H.-S. Recent Progress in Photoactive Organic Field-Effect Transistors. *Sci. Technol. Adv. Mater.* **2014**, *15*, 024202.
- (4) Muccini, M.; Koopman, W.; Toffanin, S. The Photonic Perspective of Organic Light-Emitting Transistors. *Laser Photonics Rev.* **2012**, *6*, 258–275.
- (5) Bisri, S. Z.; Piliago, C.; Gao, J.; Loi, M. A. Outlook and Emerging Semiconducting Materials for Ambipolar Transistors. *Adv. Mater.* **2014**, *26*, 1176–1199.
- (6) Hotta, S.; Yamao, T.; Bisri, S. Z.; Takenobu, T.; Iwasa, Y. Organic Single-Crystal Light-Emitting Field-Effect Transistors. *J. Mater. Chem. C* **2014**, *2*, 965–980.
- (7) Tandy, K.; Ullah, M.; Burn, P. L.; Meredith, P.; Nanddas, E. B. Unlocking the Full Potential of Light Emitting Field-Effect Transistors by Engineering Charge Injection Layers. *Org. Electron.* **2013**, *14*, 2953–2961.
- (8) Hsu, B. B. Y.; Duan, C.; Nanddas, E. B.; Gutacker, A.; Yuen, J. D.; Huang, F.; Cao, Y.; Bazan, G. C.; Samuel, I. D. W.; Heeger, A. J. Control of Efficiency, Brightness, and Recombination Zone in Light-Emitting Field Effect Transistors. *Adv. Mater.* **2012**, *24*, 1171–1175.
- (9) Roelofs, W. S. C.; Adriaans, W. H.; Janssen, R. A. J.; Kemerink, M.; de Leeuw, D. M. Light Emission in the Unipolar Regime of Ambipolar Organic Field-Effect Transistors. *Adv. Funct. Mater.* **2013**, *23*, 4133–4139.
- (10) Melucci, M.; Favaretto, L.; Zambianchi, M.; Durso, M.; Gazzano, M.; Zanelli, A.; Monari, M.; Lobello, M. G.; De Angelis, F.; Biondo, V.; et al. Molecular Tailoring of New Thieno(Bis)Imide-Based Semiconductors for Single Layer Ambipolar Light Emitting Transistors. *Chem. Mater.* **2013**, *25*, 668–676.
- (11) Bisri, S. Z.; Takenobu, T.; Iwasa, Y. The Pursuit of Electrically-Driven Organic Semiconductor Lasers. *J. Mater. Chem. C* **2014**, *2*, 2827–2836.
- (12) Swensen, J. S.; Soci, C.; Heeger, A. J. Light Emission from an Ambipolar Semiconducting Polymer Field-Effect Transistor. *Appl. Phys. Lett.* **2005**, *87*, 253511.
- (13) Zaumseil, J.; Friend, R. H.; Sirringhaus, H. Spatial Control of the Recombination Zone in an Ambipolar Light-Emitting Organic Transistor. *Nat. Mater.* **2006**, *5*, 69–74.
- (14) Zaumseil, J.; Donley, C. L.; Kim, J.-S.; Friend, R. H.; Sirringhaus, H. Efficient Top-Gate, Ambipolar, Light-Emitting Field-Effect Transistors Based on a Green-Light-Emitting Polyfluorene. *Adv. Mater.* **2006**, *18*, 2708–2712.
- (15) Capelli, B.; Toffanin, S.; Generali, G.; Usta, H.; Facchetti, A.; Muccini, M. Organic Light-Emitting Transistors with an Efficiency That Outperforms the Equivalent Light-Emitting Diodes. *Nat. Mater.* **2010**, *9*, 496–503.
- (16) Ullah, M.; Tandy, K.; Yambem, S. D.; Muhieddine, K.; Ong, W. J.; Shi, Z.; Burn, P. L.; Meredith, P.; Li, J.; Nanddas, E. B. Efficient and Bright Polymer Light Emitting Field Effect Transistors. *Org. Electron.* **2015**, *17*, 371–376.
- (17) Kajii, H.; Tanaka, H.; Kusumoto, Y.; Ohtomo, T.; Ohmori, Y. In-Plane Light Emission of Organic Light-Emitting Transistors with Bilayer Structure Using Ambipolar Semiconducting Polymers. *Org. Electron.* **2015**, *16*, 26–33.
- (18) Walker, B.; Ullah, M.; Chae, G. J.; Burn, P. L.; Cho, S.; Kim, J. Y.; Nanddas, E. B.; Seo, J. H. High Mobility Solution-Processed Hybrid Light Emitting Transistors. *Appl. Phys. Lett.* **2014**, *105*, 183302.
- (19) Yamada, K.; Yamao, T.; Hotta, S. Light-Emitting Field-Effect Transistors Having Combined Organic Semiconductor and Metal Oxide Layers. *Adv. Mater.* **2013**, *25*, 2860–2866.

- (20) Ullah, M.; Tandy, K.; Yambem, S. D.; Aljada, M.; Burn, P. L.; Meredith, P.; Namdas, E. B. Simultaneous Enhancement of Brightness, Efficiency, and Switching in Rgb Organic Light Emitting Transistors. *Adv. Mater.* **2013**, *25*, 6213–6218.
- (21) Muhieddine, K.; Ullah, M.; Pal, B. N.; Burn, P.; Namdas, E. B. Field-Effect Transistors: All Solution-Processed, Hybrid Light Emitting Field-Effect Transistors. *Adv. Mater.* **2014**, *26*, 6410–6415.
- (22) Seo, H.-S.; Kim, D.-K.; Oh, J.-D.; Shin, E.-S.; Choi, J.-H. Organic Light-Emitting Field-Effect Transistors Based Upon Pentacene and Perylene. *J. Phys. Chem. C* **2013**, *117*, 4764–4770.
- (23) Seo, H.-S.; An, M.-J.; Zhang, Y.; Choi, J.-H. Characterization of Perylene and Tetracene-Based Ambipolar Light-Emitting Field-Effect Transistors. *J. Phys. Chem. C* **2010**, *114*, 6141–6147.
- (24) Rost, C.; Karg, S.; Riess, W.; Loi, M. A.; Murgia, M.; Muccini, M. Ambipolar Light-Emitting Organic Field-Effect Transistor. *Appl. Phys. Lett.* **2004**, *85*, 1613–1615.
- (25) Soldano, C.; Stefani, A.; Biondo, V.; Basirico, L.; Turatti, G.; Generali, G.; Ortolani, L.; Morandi, V.; Veronese, G. P.; Rizzoli, R.; et al. ITO-Free Organic Light-Emitting Transistors with Graphene Gate Electrode. *ACS Photonics* **2014**, *1*, 1082–1088.
- (26) Toffanin, S.; Capelli, R.; Koopman, W.; Generali, G.; Cavallini, S.; Stefani, A.; Saguatti, D.; Ruani, G.; Muccini, M. Organic Light-Emitting Transistors with Voltage-Tunable Lit Area and Full Channel Illumination. *Laser Photonics Rev.* **2013**, *7*, 1011–1019.
- (27) Ullah, M.; Armin, A.; Tandy, K.; Yambem, S. D.; Burn, P. L.; Meredith, P.; Namdas, E. B. Defining the Light Emitting Area for Displays in the Unipolar Regime of Highly Efficient Light Emitting Transistors. *Sci. Rep.* **2015**, *5*, 8818.
- (28) Zhang, N.; Lin, J.; Luo, J.; Li, Y.; Gan, Z.; Fan, Y.; Liu, X. N-Channel Transparent Organic Thin-Film Transistors with Ag/LiF Bilayer Transparent Source-Drain Electrodes Fabricated by Thermal Evaporation. *Appl. Phys. Express* **2014**, *7*, 021601.
- (29) Steckler, T. T.; Lee, M. J.; Chen, Z.; Fenwick, O.; Andersson, M. R.; Cacialli, F.; Sirringhaus, H. Multifunctional Materials for OFETs, LEFETs and NIR PLEDs. *J. Mater. Chem. C* **2014**, *2*, 5133–5141.
- (30) Ikezoe, I.; Tanaka, H.; Hiraoka, K.; Kajii, H.; Ohmori, Y. Influence of Source/Drain Electrodes on External Quantum Efficiency of Ambipolar Organic Light-Emitting Transistors. *Org. Electron.* **2014**, *15*, 105–110.
- (31) Gwinner, M. C.; Kabra, D.; Roberts, M.; Brenner, T. J. K.; Wallikewitz, B. H.; McNeill, C. R.; Friend, R. H.; Sirringhaus, H. Highly Efficient Single-Layer Polymer Ambipolar Light-Emitting Field-Effect Transistors. *Adv. Mater.* **2012**, *24*, 2728–2734.
- (32) Capelli, R.; Dinelli, F.; Loi, M. A.; Murgia, M.; Muccini, M. Ambipolar Light-Emitting Field-Effect Transistors Based on Molecular Thin Films. *Proc. of SPIE* **2006**, 6333, 63330T.
- (33) Madigan, C. F.; Lu, M. H.; Sturm, J. C. Improvement of Output Coupling Efficiency of Organic Light-Emitting Diodes by Backside Substrate Modification. *Appl. Phys. Lett.* **2000**, *76*, 1650–1652.
- (34) Namdas, E. B.; Hsu, B. B. Y.; Liu, Z.; Lo, S.-C.; Burn, P. L.; Samuel, I. D. W. Phosphorescent Light-Emitting Transistors: Harvesting Triplet Excitons. *Adv. Mater.* **2009**, *21*, 4957–4961.
- (35) Chang, C.-H.; Wu, Z.-J.; Liang, Y.-H.; Chang, Y.-S.; Chiu, C.-H.; Tai, C.-W.; Chang, H.-H. Aligned Energy-Level Design for Decreasing Operation Voltage of Tandem White Organic Light-Emitting Diodes. *Thin Solid Films* **2013**, *548*, 389–397.
- (36) Yang, C.-H.; Tai, C.-C.; Sun, I.-W. Synthesis of a High-Efficiency Red Phosphorescent Emitter for Organic Light-Emitting Diodes. *J. Mater. Chem.* **2004**, *14*, 947–950.
- (37) Lepeltier, M.; Dumur, F.; Wantz, G.; Vila, N.; Mbomekallé, I.; Bertin, D.; Gigmes, D.; Mayer, C. R. Red Phosphorescent Organic Light-Emitting Diodes (PhOLEDs) Based on a Heteroleptic Cyclo-metallated Iridium(III) Complex. *J. Lumin.* **2013**, *143*, 145–149.
- (38) Yang, J.-P.; Xiao, Y.; Deng, Y.-H.; Duhm, S.; Ueno, N.; Lee, S.-T.; Li, Y.-Q.; Tang, J.-X. Electric-Field-Assisted Charge Generation and Separation Process in Transition Metal Oxide-Based Interconnectors for Tandem Organic Light-Emitting Diodes. *Adv. Funct. Mater.* **2012**, *22*, 600–608.
- (39) Keum, C. M.; Lee, I. H.; Lee, S. H.; Lee, G. J.; Kim, M. H.; Lee, S. D. Quasi-Surface Emission in Vertical Organic Light-Emitting Transistors with Network Electrode. *Opt. Express* **2014**, *22*, 14750–14756.
- (40) Nakamura, K.; Hata, T.; Yoshizawa, A.; Obata, K.; Endo, H.; Kudo, K. Metal-Insulator-Semiconductor-Type Organic Light-Emitting Transistor on Plastic Substrate. *Appl. Phys. Lett.* **2006**, *89*, 103525.